

Cell divisions imprint long lasting elastic strain fields in epithelial tissues

Ali Tahaei,¹ Romina Pisticello-Gómez,² S Suganthan,¹ Greta Cwikla,³

Jana F. Fuhrmann,^{2,3} Natalie A. Dye,^{2,3} and Marko Popović^{1,3,4}

¹Max Planck Institute for the Physics of Complex Systems, Nöthnitzer Str.38, 01187 Dresden, Germany

²Max Planck Institute for Molecular Cell Biology and Genetics,
Pfotenhauerstrasse 108, Dresden, 01307, Germany

³Excellence Cluster, Physics of Life, Technische Universität Dresden, Arnoldstrasse 18, Dresden, 01307, Germany

⁴Center for Systems Biology Dresden, Pfotenhauerstrasse 108, 01307 Dresden, Germany

A hallmark of biological tissues, viewed as complex cellular materials, is the active generation of mechanical stresses by cellular processes, such as cell divisions. Each cellular event generates a force dipole that deforms the surrounding tissue. Therefore, a quantitative description of these force dipoles, and their consequences on tissue mechanics, is one of the central problems in understanding the overall tissue mechanics. In this work we analyze previously published experimental data on fruit fly *D. melanogaster* wing epithelia to quantitatively describe the deformation fields induced by a cell-scale force dipole. We find that the measured deformation field can be explained by a simple model of fly epithelium as a linearly elastic sheet. This fact allows us to use measurements of the strain field around cellular events, such as cell divisions, to infer the magnitude and dynamics of the mechanical forces they generate. In particular, we find that cell divisions exert a transient isotropic force dipole field, corresponding to the temporary localisation of the cell nucleus to the tissue surface during the division, and traceless-symmetric force dipole field that remains detectable from the tissue strain field for up to about 3.5 hours after the division. This is the timescale on which elastic strains are erased by other mechanical processes and therefore it corresponds to the tissue fluidization timescale. In summary, we have developed a method to infer force dipoles induced by cell divisions, by observing the strain field in the surrounding tissues. Using this method we quantitatively characterize mechanical forces generated during a cell division, and their effects on the tissue mechanics.

I. INTRODUCTION

How mechanical forces influence biological tissues is one of the central problems in animal development and regeneration [1–5]. Biological tissues are often described as soft viscoelastic materials [6] that are elastic on sufficiently short timescales. Tissue fluidization on longer timescales arises from cell divisions, extrusions and intercalations, that restructure the tissue over time [7–10].

Cell divisions are an intrinsic source of mechanical force generation within tissues. When a cell divides, particularly in a closely packed epithelium, it induces deformation in the surrounding tissue [11, 12], potentially leading to cellular rearrangements [13] and contributing to the overall tissue flow [7, 14, 15]. Furthermore, cell divisions have been indicated to control the glassy cell dynamics observed in cultured epithelial tissues [16, 17] and explanted embryonic tissues [18]. However, despite the fact that cell divisions are a hallmark of biological matter and seem to be major factor in controlling material properties of biological tissues, quantitative understanding of the mechanical forces generated by cell divisions and their immediate consequences on the surrounding tissue is still lacking.

In order to study the mechanics of cell divisions, we need to probe mechanical stresses in the surrounding tissue. One of the most common methods of probing mechanical stresses is the laser ablation experiment, in which one or multiple cells are destroyed by a laser. The resulting displacement of the ablated tissue boundary re-

flects the pre-stresses existing in the tissue before the ablation [8, 19–23]. Information about the pre-stresses are extracted either from the initial dynamics of tissue boundary displacement [20, 22] or from the final relaxed shape of the tissue [19, 21, 23, 24]. Previous analyses focused on changes in position or shape of specific points or outlines in the vicinity of the ablation. Therefore, they could not provide an insight into the strain field induced in the surrounding tissue, and they had to rely on assumptions about tissue mechanical properties. Furthermore, to extract information about all components of the pre-stress in the tissue, previous methods require a precise, circular laser ablation [21, 24]. If we could instead infer force dipoles induced by cellular processes such as cell divisions, we would be able to extract information about tissue mechanics in a completely non-invasive way. Such a method was recently developed to infer the properties of the core of plastic particle rearrangements in computer glasses [25, 26]. Therefore, the starting point of our work, on the way to study cell division mechanics, is to develop a method that allows us infer the force dipole in an epithelial tissue from the tissue strain field.

In this work, we first provide a detailed quantitative analysis of the tissue displacement field following a linear laser ablation performed in the pupal wing epithelium of the fruit fly *D. melanogaster*. We show that the response of the fly wing epithelium to a laser ablation is consistent with that of a two-dimensional linear elastic sheet. This allows us to infer the force dipole induced by the ablation, normalized by the elastic constant, from the observed strain field. Furthermore, by analyzing the

dynamics of the strain field, we show that the dominant mode of dissipation in the fly wing epithelium on short timescales of 1s to 50s is the viscous dissipation, as opposed to frictional dissipation with a substrate.

Using our method to infer force dipole from its strain field, we determine the force dipole generated by cell divisions in the *D. melanogaster* wing disc. We find that the isotropic component of the cell division force dipole tensor is only transient and vanishes almost immediately after the division, indicating that no net cell growth is accumulated during the cell division. Furthermore, we find that the traceless-symmetric component of the force dipole, imprinted by the cell division, remains visible in the surrounding tissue for up to about 3.5 hours after the division. This provides a measurement of the fluidization timescale in the tissue, and demonstrates importance of elastic interactions in tissue-scale morphogenetic processes that take place on a comparable timescale, such as wing disc eversion [27].

II. THE FRUIT FLY WING EPITHELIUM IS A 2D LINEAR ELASTIC SHEET

A. Linear laser ablation experiments

Linear laser ablation experiments, during which a small linear segment of tissue is destroyed by a laser, have been performed in the *D. melanogaster* wing epithelium during pupal morphogenesis [23]. To obtain information about the pre-stress in the tissue, the dynamics of the closest cell-cell junction was measured as it retracted away from the ablation. Here, we use movies of laser ablation experiments published in Ref. [23] to study the deformation in the tissue surrounding the laser ablation. An example of such a laser ablation experiment is shown in Fig. 1 (A.i), where the red line indicates the line ablated by the laser. Following the ablation, the tissue relaxes until reaching a mechanical equilibrium after at most $T_e = 50s$ in Fig. 1 (A.ii), see Methods.

To measure the tissue strain field, we segmented the apical cell surfaces over time and quantified the area a and the elongation tensor Q_{ij} of each cell, which quantifies its shape [8, 28]. Since no cell divisions or rearrangements appear in the region of interest following the laser ablation, we quantify the tissue strain field $U_{ij}(\mathbf{r}, t)$ from the change in cell shape and size relative to their values before the ablation, see Methods. The strain field tensor consists of the isotropic strain component U_{kk} and traceless-symmetric component \tilde{U}_{ij} which we denote as pure shear strain component. In Fig. 1 (A.iv) we show the pure shear strain field component \tilde{U}_{xy} at 100s after the laser ablation, which exhibits a clear spatial pattern, see SI Fig. 2 (A) for the other traceless-symmetric component and isotropic component of experiment 1 and SI Fig. 3 (A) for all components of the experiment 2.

Our goal is to find the relationships between the induced strain field and the forces induced by the ablation.

Since the process of ablation does not introduce any net force, the dominant component of the induced force field will be dipolar. Therefore, we aim to relate components of the strain field at distance \vec{r} from the ablation to the components of the force dipole tensor, as illustrated in Fig. 1 (B.i,ii).

We first consider tissue strain after it has reached the mechanical equilibrium after the time T_e and calculate the discrete angular Fourier spectrum $\tilde{U}_{ij}^{ss}(\mathbf{r}, m)$, where $r = |\mathbf{r}|$ is distance from the center of ablation and m is the angular mode index, see Methods. We find the strongest signal in the second and the fourth mode of the pure shear strain components, see Fig. 1 (C.i) and SI Fig. 2 (B.ii), which correspond to $\cos(2\varphi)$ and $\cos(4\varphi)$ angular Fourier modes. In the isotropic strain component we find the strongest signal in zeroth and second mode, see SI Fig. 2 (B.i), which correspond to the constant and $\cos(2\varphi)$ angular Fourier modes. We then quantified the radial dependence of the second angular mode and we find that its magnitude decays as r^{-2} , as shown in Fig. 1 (C.ii). These results reminded us of the far field of Eshelby propagators in two-dimensional linear elastic sheets [25, 29, 30] and we next tested whether linear elastic theory can indeed quantitatively account for our measurements.

We briefly present linear elastic theory of a sheet in which a point force dipole has been inserted. A force dipole is represented by a tensor D_{ij} that can be decomposed into isotropic and traceless-symmetric contributions $D_{ij} = D_0\delta_{ij} + \tilde{D}_{ij}$ [31]. Inserting a force dipole in an elastic sheet induces a strain field that is determined by the force balance equation

$$\partial_j \sigma_{ij} + \partial_j (\delta(\mathbf{r}) D_{ij}) = 0 \quad (1)$$

where σ_{ij} is the stress tensor in the elastic sheet, which can be decomposed into pressure P and shear stress $\tilde{\sigma}$: $\sigma_{ij} = -P\delta_{ij} + \tilde{\sigma}_{ij}$. The resulting strain field can be written as

$$u_{ij}(\mathbf{r}) = G_{ijkl}(\mathbf{r}) D_{kl}, \quad (2)$$

where G_{ijkl} is the elastic dipole propagator and \mathbf{r} is the distance from the force dipole, see SI. We graphically illustrate the components of Eq. 2 in Fig. 1 (B.iii), using the Voigt tensor representation. In this representation, the force dipole propagator elements are organised in a matrix, which we plot in Fig. 1 (b). From this point, we use the normalised force dipole defined as $d_{ij} = D_{ij}/(2\pi K(1 + \mu))$. The propagator elements depend only on $\cos(2\varphi)$, $\sin(2\varphi)$, $\cos(4\varphi)$ and $\sin(4\varphi)$, see Fig. 1 (B.iii) and SI, consistent with the observed second and fourth angular Fourier modes in the data. Furthermore, all components of G_{ijkl} decay in space as r^{-2} . This is consistent with the radial profile observed in the experimental data for $m = 2$ modes, see Fig. 1 (C.ii) and SI Fig. 4. Radial profile of $m = 4$ modes decay faster and appear to be much more susceptible to the noise in the data. Therefore, the strain field measured in the laser

ablation experiments is consistent with a linear elastic response of the tissue to the force dipoles generated by the ablation. However, to confirm this hypothesis, we need to show that linear elastic theory can quantitatively account for the observed strain fields.

We fit the steady state tissue strain field U_{ij}^{ss} with a strain field predicted by a linear elastic theory of a two-dimensional elastic sheet in Eq. 2. The fitting parameters are the three independent components of the force dipole tensor and the ratio μ of the two-dimensional shear and bulk elastic moduli. By analysing two laser ablation experiments, we find that the data are well described by the fit, as shown in Fig. 1 (D) and SI Fig. 5. The fitting parameters are consistent between the two experiments, see Table 1, except \tilde{d}_{xx} , which varies by a factor of two. This shows that there is a difference in the force dipole magnitude generated by the ablation, which could arise either from a difference of tissue pre-stresses or a difference in the effective ablation size in the two experiments. Furthermore, the ratio $\mu \approx 2$, corresponding to the Poisson ratio of $\nu \approx -0.33$, is comparable with the value $\mu \approx 3$, corresponding to the Poisson ratio of $\nu \approx -0.5$, recently reported in the same tissue using a laser ablation method based on circular ablation shape [23].

To further test our analysis of the laser ablation experiments, we simulate a linear ablation in the vertex model of epithelial tissues [19]. We remove two cells from a pre-stressed cellular network, see SI, and then we quantify the resulting strain. We find that the simulation shows the same pattern as in experiments, consistent with the linear elastic theory of a 2-d sheet Fig. 1 (E, F) and SI Fig. 6. We fit the linear elastic theory to the observed strain field pattern and infer the force density generated by the ablation from tissue deformation. Finally, we find the Poisson's ratio of the vertex model cellular network to be $\nu = -0.061 \pm 0.005$. This finding is consistent with the value predicted value $\nu \approx -0.060$ in Ref. [32] for the vertex model parameters we use, see SI.

Our results show that response of the *D. melanogaster* wing epithelium to a small linear laser ablation is consistent with that of a linearly elastic sheet with a negative two-dimensional Poisson ratio. This allows us to infer the force dipole tensor induced by the ablation from the tissue strain field, which we confirmed using the vertex model simulations.

B. Viscous dissipation determines tissue relaxation dynamics

Our analysis of the strain in the ablated tissue after it has relaxed allowed us to study its elastic properties. Now, we explore dynamics of tissue strain as it approaches the equilibrium, which will allow us to study dissipative processes in fly wing epithelium. We consider two possible dissipation mechanisms: viscosity and friction with a substrate.

Interestingly, in a continuum model of a tissue as an

elastic sheet, these two dissipation mechanisms lead to qualitatively different relaxation dynamics upon insertion of a force dipole. In particular, in an elastic sheet with only viscous dissipation, all strain field components decays as $1/r^2$ with the distance from the force dipole throughout the relaxation with the amplitude evolving in time, see SI and Fig. 2 (A.i). However, in an elastic sheet with only frictional dissipation, the strain field propagates through the sheet: at distances smaller than the propagation front, the strain field converges to the steady state solution and rapidly decays beyond the front, see SI and Fig. 2 (A.ii).

To quantify the dynamics of tissue relaxation following the laser ablation, we measure the strain field in time intervals of 4.5s, starting from 1s after the ablation, (SI Fig. 7). We find that the angular strain pattern is the same as in the mechanical equilibrium one, see Movie 1. We analyse the dynamics of the strain radial profile by calculating the second angular Fourier mode of the strain field at all measured timepoints, see Fig. 2 (B.i) and SI Fig. 7. We find that at all timepoints the strain field is consistent with $1/r^2$ decay and we do not see any signature of a propagating front, see Fig. 2. Therefore, we conclude that the viscosity is the dominant mode of dissipation in the fly wing epithelium on timescales above 1s, corresponding to the initial timepoint we observe after the ablation, and below $T_e \approx 50s$.

To make sure that a predicted propagation front could be observed in presence of frictional dissipation we performed vertex model simulations of laser ablation that include only the frictional dissipation, see SI for details. We indeed find a clear propagation of the strain field that converges to the steady state value as the propagation front expands (2 (B.ii) and SI Fig. 8), as predicted by the analytical calculation (2 (A.ii)).

TABLE I. Parameters obtained by fitting the continuum theory to spatio-temporal pattern of strain field accumulated in the tissue after the ablation.

exp.	d_0 [μm] ²	\tilde{d}_{xx} [μm] ²	\tilde{d}_{xy} [μm] ²	μ	τ_1 (s)	τ_2 (s)
1	16 ± 1	15 ± 1	2 ± 1	1.9 ± 0.1	11 ± 1	12 ± 1
2	15 ± 2	31 ± 2	0 ± 2	2.1 ± 0.3	48 ± 2	55 ± 2

Our continuum model of an elastic sheet provides the dynamical strain propagator $G_{ij}(\mathbf{r}, t) = G_{ij}(\mathbf{r})T_{ij}(t)$, where no sum over repeated indices is performed. $G_{ij}(\mathbf{r})$ is the steady state propagator, and $T_{ij}(t)$ is the relaxation matrix whose components contains two relaxation factors $g_1(t) = 1 - \exp(-t/\tau_1)$ and $g_2(t) = 1 - \exp(-t/\tau_2)$, where the two relaxation timescales

$$\tau_1 = \frac{\bar{\eta}}{\bar{K}} \frac{1 + 2\eta/\bar{\eta}}{1 + \mu} \quad (3)$$

$$\tau_2 = \frac{\eta}{K} \quad (4)$$

are related to the bulk and shear elastic constants, and bulk and shear viscosities \bar{K} , $2K$, $\bar{\eta}$, and 2η , respectively

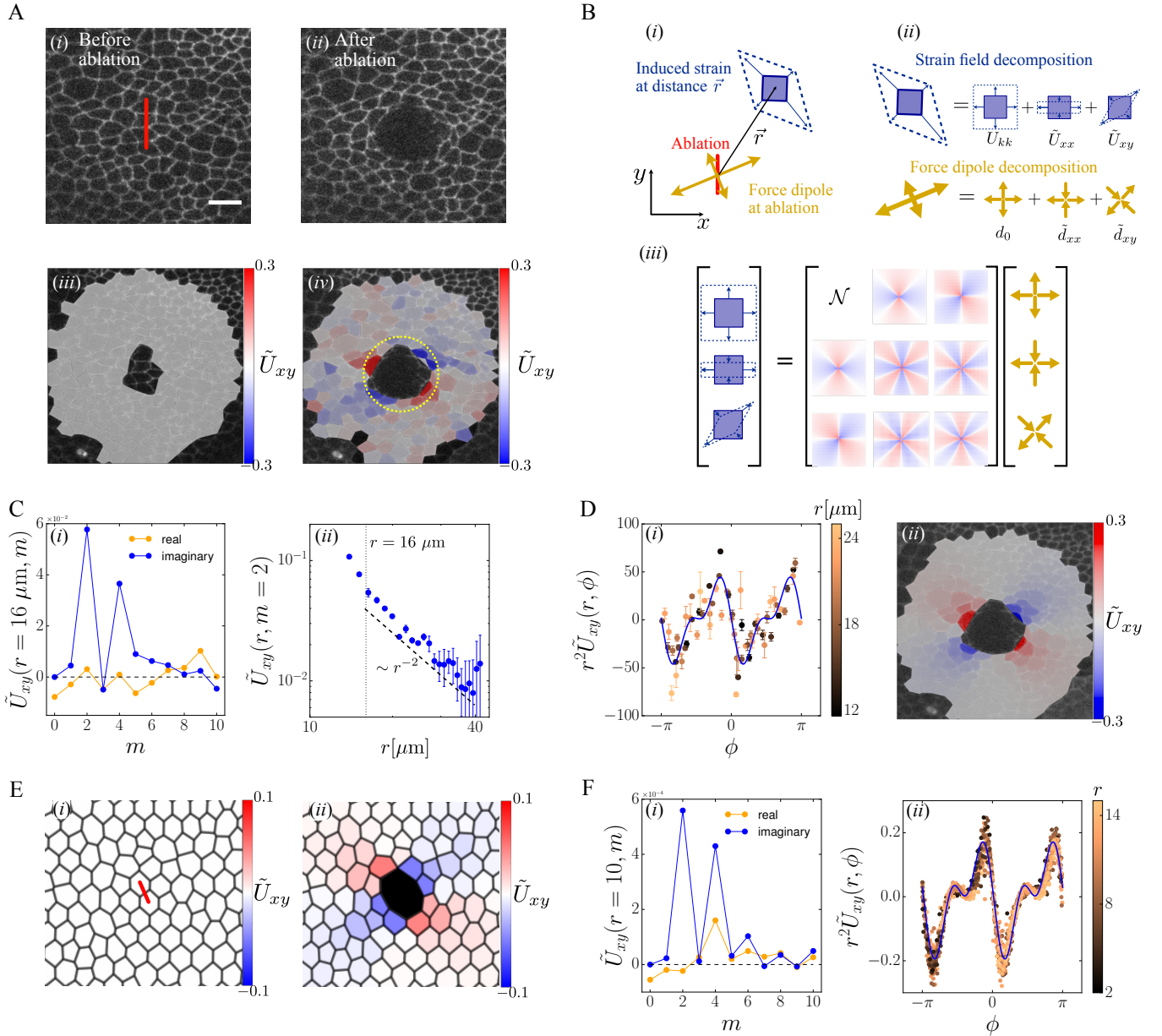


FIG. 1. (A.i) Fluorescently labeled cell outlines show the cellular packing before the laser ablation. The red bar indicates the location that will be ablated. (A.ii) Following the laser ablation tissue has deformed away from the ablated region. (A.iii) The cells we have tracked and segmented define the region of interest colored in white. (A.iv) In the region of interest, we show the accumulated cell strain component \tilde{U}_{xy} . The scale bar is $10 \mu\text{m}$. (B.i) A force dipole in a two dimensional linear elastic system induces a strain in distance \vec{r} . (B.ii) Two dimensional strain field and force dipole tensors are decomposed into isotropic and traceless-symmetric components. (B.iii) A Voigt representation of the relation between strain at position \vec{r} induced by a force dipole at the origin. (C.i) Angular Fourier modes of \tilde{U}_{xy} at distance $r = 16 \mu\text{m}$, which corresponds to the yellow circle A.iv, shows a clear signal in modes $m = 2$ and $m = 4$ modes. (C.ii) The radial profile of the $m = 2$ angular mode shows a radial profile consistent with r^{-2} (dashed line). The dotted line indicates the distance $r = 16 \mu\text{m}$. (D.i) Fit of the linear elastic theory to the experimental data. The solid blue line is the fitted strain field with the corresponding fit parameters reported in Table I, exp. 1. (D.ii) Visualisation of the fitted strain field. (E.i) The cellular network of tissue in the vertex model simulation. The red bar indicates two cells removed by an ablation. (E.ii) The cell strain field accumulated in the tissue after the ablation. (F.i) Angular Fourier modes of the strain field pattern in E.ii showing peaks in the second and fourth modes. (F.ii) Fit of the linear elastic theory to cell strain field in the vertex model. The solid blue is the fitted strain field with the fit parameters $d_0 = (10.92 \pm 0.01) \times 10^{-2} a_0$, $\vec{d}_{xx} = (8.29 \pm 0.01) \times 10^{-2} a_0$, $\vec{d}_{xy} = (2.93 \pm 0.01) \times 10^{-2} a_0$ and $\mu = 1.13 \pm 0.01$.

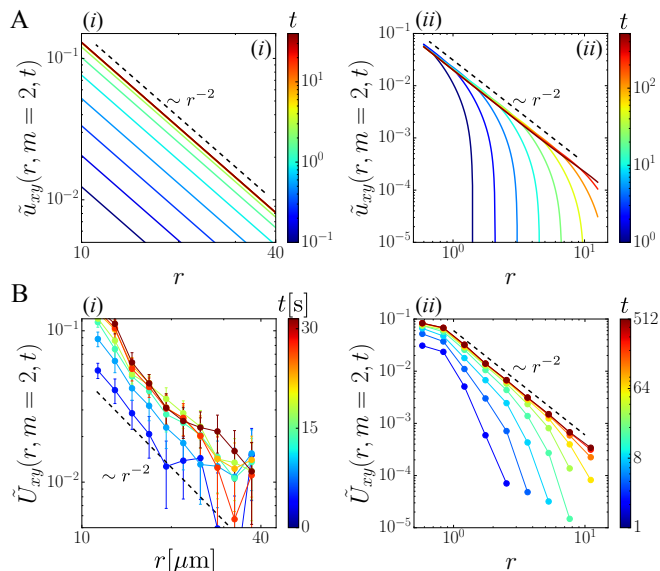


FIG. 2. Time evolution the second Fourier mode $m = 2$ of the strain field xy component induced by a force dipole for: (A.i) linear elastic sheet with viscous dissipation, (A.ii) linear elastic sheet with frictional dissipation, (B.i) laser ablation experiment (B.ii) vertex model simulation with frictional dissipation. Dashed line indicates the power-law r^{-2} decay for reference.

(see SI). To extract τ_1 and τ_2 from experimental data, as described in SI and shown in SI Fig. 1. We find that the two relaxation timescales are very similar, although they vary between experiments, see Table 1. It is at the moment unclear whether the difference between the relaxation timescales in two experiments stems from variability of elastic constants or viscosity, or some other factor. While this will be an important open question to resolve in future, further investigation of relaxation timescale variability is beyond the scope of this work.

So far, our detailed analysis of the strain in the fly wing epithelium in response to the laser ablation shows that the tissue behaves as a two-dimensional viscoelastic solid. With this knowledge in hand, we can now infer force dipoles generated by cell divisions, and thereby study their mechanics, by simply observing the dynamics of the surrounding tissue strain caused by the division, without the need to directly perturb the tissue.

III. ELASTIC DEFORMATION IMPRINTED BY A CELL DIVISION

Cell division is a complex process during which the mother cell is split into two daughter cells. Here, we aim to characterise the mechanical forces generated by the dividing cell by analysing the strain field a dividing cell induces in the fly wing epithelium.

We analysed cell divisions in previously published experiments [24] on explanted *D. melanogaster* wing imag-

inal discs [33]. Wing discs were cultured over about 13 hours, during which the tissue was imaged every 5 minutes, and individual cells were segmented and tracked over time. The progress of a typical cell division is shown in Fig. 3 (A). Before the actual cell division, the mother appears to inflate Fig. 3 (A.ii), which is not a real increase in cell size, but is rather a consequence of the cell nucleus arriving to the apical surface of the cell to divide [11, 34]. This transient inflation is followed by the creation of the new cell boundary, and the two daughter cells become visible Fig. 3 (A.iii). For each cell division, we define the time of the new bond creation as the reference cell division time $t = 0$.

Fig. 3 (A.iv) qualitatively summarizes these experimental observations. For each cell division, we quantify the tissue strain field in the vicinity of the dividing cell, as described in Section II, relative to the starting timepoint $t_0 = -60$ min before the cell division time. We show an example of the cell strain field induced by a dividing cell in Fig. 3 (B). The timescale on which the cell division forces evolve, which is on the order of tens of minutes, is much larger than the relaxation timescale extracted in Section II, which is below one minute. Therefore, the observed strain field dynamics is largely due to changes of the force dipole generated by the cell division, and not due to much faster stress propagation through the tissue.

We find that a single cell division generates weaker forces compared to those induced by laser ablation (compare Fig. 1 A and Fig. 3 B), and the corresponding strain field is more susceptible to noise. Therefore, we average the strain field from multiple cell divisions ($N = 682$). We first align the centers of the cell division, defined as the area weighted average of daughter cell centers at the cell division time ($t = 0$). We next rotate each division such that the orientation of the line connecting daughter cell centers is oriented along the x -axis at the cell division time. We show the resulting strain field component \tilde{U}_{xy} in Fig. 3 (C) at times $t = -20$ min, corresponding to the peak of the cell inflation, and $t = 30$ min after the cell division. In Fig. 3 (C.i), the 2-fold symmetry of the angular strain pattern indicates that the isotropic force dipole is dominant, consistent with the isotropic cell inflation. In Fig. 3 (C.ii), the pattern is closer to 4-fold symmetric one, such as would be induced by an anisotropic force dipole.

We fit the linear elastic theory Eq. 2 to the experimentally measured strain field at each time point and extract the resulting force dipole $d_{ij}(t)$. We find that the isotropic force dipole component d_0 rises sharply during the mother cell inflation and peaks at about $t = -20$ min (magenta line in Fig. 3 D). However, by the time of the new bond formation, the isotropic component has disappeared and remains negligible at later times. This result shows that cell does not noticeably grow during the division, but rather that the division reorganises the available material into the two daughter cells. The traceless part of the force dipole \tilde{d}_{xx} grows as the new bond is formed and persists in the tissue multiple hours after the divi-

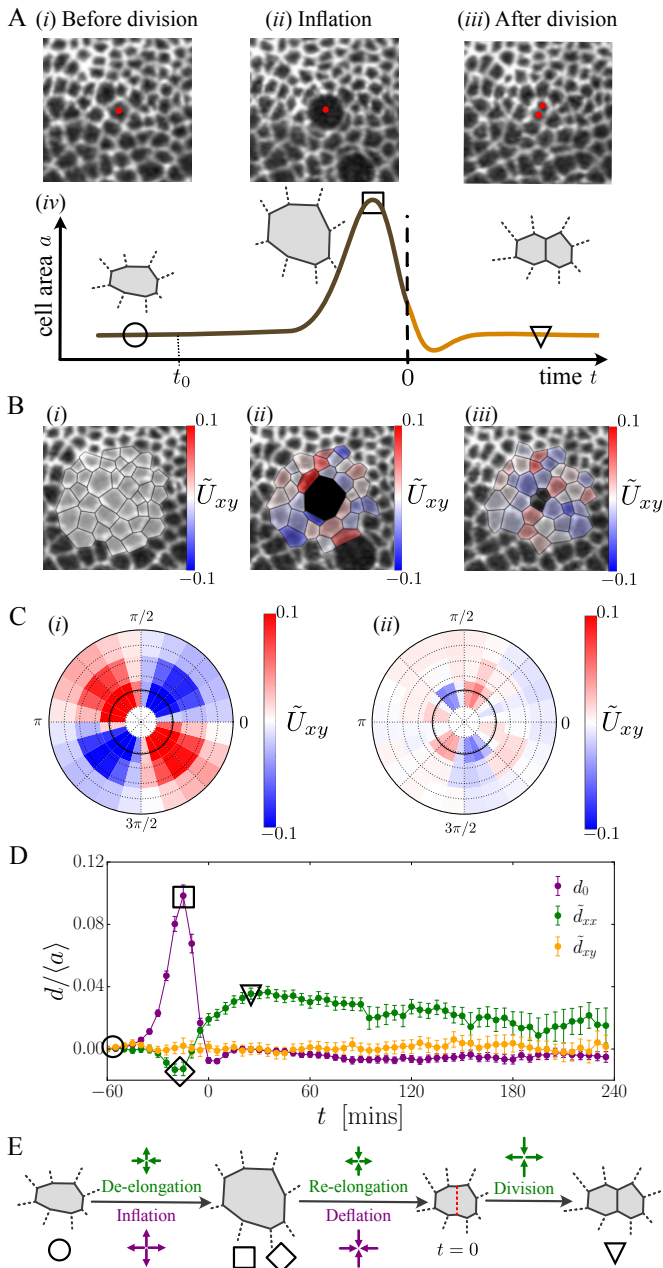


FIG. 3. (A) Snapshots of a cell division in three stages. (A.i) As the mother cell starts the division process, (A.ii) it rounds up, corresponding to the inflation, then (A.iii) it shrinks and divides into the daughter cells. The red dots show the mother and the daughter cells. (A.iv) A schematic representation of the cell area of the mother cell (brown) and the daughter cells (orange) during the division process. The symbols highlight the stage of the dividing cell before the division, at the peak of inflation, and after the division. The new bond forms at $t = 0$, and t_0 is the reference state. (B) Strain \tilde{U}_{xy} of the cells near a typical cell division at the three stages shown in (A) with $t_0 = -60$ [min]. (C) Ensemble average ($N = 682$) of \tilde{U}_{xy} around the dividing cell: (C.i) at the peak of the inflation $t = -20$ [min] (corresponding to (A.ii) and (B.ii)), and (C.ii) after the division $t = 30$ [min] (corresponding to (A.iii) and (B.iii)). (D) The force dipole generated by a cell division as a function of time. (E) A schematic summary of the force dipoles during stages of a cell division.

tion (green line in Fig. 3 D), indicating that the division-induced strains remain imprinted in the tissue long after the division has been executed. Over time, \tilde{d}_{xx} slowly decays while its fluctuations increase, representing the effect of other cell divisions and rearrangements that appear in the tissue. We estimate the tissue fluidization time from the decay of \tilde{d}_{xx} in time by fitting an exponential function to it. We find the fluidization timescale to be $\tau_\alpha \simeq 3.5 \pm 0.7$ minutes, over which \tilde{d}_{xx} vanishes and, therefore, the strain field induced by the division is erased. Note that component \tilde{d}_{xy} remains negligible at all times.

Finally, we note that at the time of the peak of d_0 , there is a small but clear negative peak in \tilde{d}_{xx} . To interpret this observation, we have to remember that our strain measurements are relative to the state of the cells at $t_0 = -60$ min. Since the mother cell attains an almost perfectly circular shape during the inflation, any initial anisotropy of the mother cell at time t_0 gives rise to an anisotropic force dipole component during the inflation. Therefore, the observed negative value of \tilde{d}_{xx} indicates that mother cells are slightly elongated along the future division axis, consistent with the well known Hertwig's rule [11, 35–38]. We summarise these results in Fig. 3 (E).

IV. DISCUSSION

In this work, we devised a full spatio-temporal analysis of tissue strain induced by two types of force dipole fields: linear laser ablations and cell divisions. In this way, we have shown that the developing *Drosophila* wing epithelium behaves as a two-dimensional elastic solid with viscous dissipation. We also measured its two-dimensional Poisson ratio, which we find to be negative, consistent with the values reported in the literature [23, 24].

We characterized the dynamics of mechanical forces generated by a dividing cell throughout the cell division process. We found that strain fields imprinted by a cell division are slowly erased on the timescale of $\tau_\alpha = 3.5 \pm 0.7$ hr, which can be understood as a fluidization timescale of the *Drosophila* wing tissue. Furthermore, our analysis shows that there is no cell growth during a division and stresses induced by the cell division correspond to those of a pure shear force dipole. Finally, we found that Hertwig's rule applies in the *D. melanogaster* wing disc [11, 12].

An important implication of our work is that the *Drosophila* wing epithelium is a solid whose fluidization time τ_α is not negligible on the developmental timescales. For example, large scale shape changes that the wing undergoes during eversion are executed on a similar timescale [27]. A possible physical picture of the *Drosophila* wing epithelium that could account for our observations, is that of a glassy material, or as was put forward in glass literature, a solid that flows [39–41]. In other words, the long-range elastic interactions between

cells would lead to correlated glassy dynamics, which has been reported in tissue cultures [16, 17], and it remains to be seen whether they indeed play a role in developing tissues. In summary, our results quantify force dipoles generated by dividing cells in developing *D. melanogaster* wing epithelia, as well as elastic interactions between cells, which paves the way to development tissue mechanics theory and motivates further experimental study of collective cell dynamics.

ACKNOWLEDGEMENTS

We would like to thank Michael Staddon, Frank Jülicher, Jonas Neipel for useful discussions and comments. NAD, JFF, and GC acknowledge funding from the Max Planck Society, Excellence Cluster Physics of Life (EXC-2068-390729961), Deutsche Forschungsgemeinschaft (SPP1782/EA4/10-2), Deutsche Krebshilfe/MSNZ Dresden.

V. METHODS

A. Cell segmentation and tracking

The linear ablation experiments came from the pupal morphogenesis stage and were previously published in Ref. [23], where the authors analyzed initial retraction velocity of the ablated bonds. Here, we took these experiments and fully segmented and tracked cells in the entire field using the FIJI plugin, TissueAnalyzer [42], using a bond cutoff of 2 pixels. Then, after the manual correction of segmentation errors, we use TissueMiner [43] to analyse changes in the cell shape and size.

The cell division experimental data came from the wing disc stage and was previously segmented, tracked and analyzed in Ref. [24, 44].

B. Tissue relaxation after a laser ablation

After the ablation, nearby tissue relaxes to the new mechanical equilibrium. However, beyond 2 minutes after the ablation we observed additional motion of the tissue which we interpret as the onset of the wound healing response in the tissue. In this study, we are interested in the stress released by the ablation in the tissue, not the wound healing process, and therefore we limit our analysis to times up to 2 minutes after the laser ablation.

C. Tissue strain field measurement

Strain field consists of isotropic strain $U_{kk}(\mathbf{r}, t)/2$ and shear strain $\tilde{U}_{ij}(\mathbf{r}, t)$. To measure the strain field in the tissue we calculate the change in cell shape and size as

described in [28, 45] at each timepoint. Since there are no cell rearrangements and divisions we estimate the accumulated tissue shear strain field in a cell from the difference between the cell shape tensors

$$\tilde{U}_{ij}(t) \simeq Q_{ij}(t) - Q_{ij}(0) \quad (5)$$

The only approximation is that we neglect to account for change in cell elongation due to local rotations. We determined the exact cell shear tensor at several timepoints and we found that the difference from our approximation are small. Therefore, we use the approximate expression for simplicity. We estimate the isotropic strain field in a cell from the change in cell area a

$$U_{kk}(t) = \log \left(\frac{a(t)}{a(0)} \right). \quad (6)$$

We define the tissue strain field $U_{ij}(\mathbf{r}, t)$ at position \mathbf{r} to have the value of the strain tensor obtained for the cell inside of which point \mathbf{r} lies.

D. Discrete angular Fourier transform

To investigate the angular pattern of the strain field and study its radial profiles, we look at the angular discrete Fourier transformation of the tissue strain field. The strain in position \mathbf{r} is given by $U_{ij}(r, \varphi)$ where r is the distance to the center of the cut and φ is the polar angle. We use the notation $U_{ij}(r, m)$ for the m -th angular mode of discrete angular Fourier transform at a distance r , and it is defined as,

$$U_{ij}(r, m) = \frac{1}{N} \sum_{i=1}^N U_{ij}(r, \varphi_i) e^{im\varphi_i}, \quad (7)$$

where φ_i s are N uniformly distributed number between 0 and 2π .

E. Fit of the elastic theory to data

We measure force dipole, the ratio of shear modulus to bulk modulus, and viscosity by fitting the strain field pattern to the elastic and viscoelastic theories. First, we define a cost function

$$E = \sum_{\alpha \in \text{cells}} \left[(U_{kk}^{\alpha} - u_{kk}(\mathbf{r}^{\alpha}))^2 + (\tilde{U}_{xx}^{\alpha} - \tilde{u}_{xx}(\mathbf{r}^{\alpha}))^2 + (\tilde{U}_{xy}^{\alpha} - \tilde{u}_{xy}(\mathbf{r}^{\alpha}))^2 \right], \quad (8)$$

where U_{ij}^{α} is the cell strain measured from data, \mathbf{r}^{α} is the position of centre of each cell and $u_{ij}(\mathbf{r}^{\alpha})$ is the strain field predicted from theory in position \mathbf{r}^{α} . By minimizing E , we find the force magnitude of the force dipole, the ratio of the shear modulus to bulk modulus, and the

relaxation timescales. In the elastic case, first, we minimise a steady state signal to find μ then we fix μ and repeat the minimisation process to find d_{ij} . In viscoelastic case, we use μ and d_{ij} from the steady state elastic response, then we minimise E at different time points to find $T_{ij}(t)$.

To analyse cell divisions, we first choose timepoint $t = 25$ min and change the reference time t_0 from -120 to -40 . We fit the data for different t_0 in that range and obtain corresponding set of $\mu(t_0)$ values. We determine the parameter μ as the average $\langle\mu(t_0)\rangle$ and we do not vary it in subsequent fitting of the strain field. Then,

to determine the force dipole at each timepoint t we fix $t_0 = -60$ min fit the theory to the data to find the force dipole at different time points.

F. Estimation of the tissue fluidization time

To measure the decay time scale of the anisotropic force dipole \tilde{d}_{xx} , we fit an exponential function to normalized force dipole $y = \tilde{d}_{xx}(t)/\langle a \rangle$ as $f(y) = \tilde{d}_{xx}(t = 0) \exp[-t/\tau_\alpha]$ to observed data in Fig. 3 (D). From that, we obtain the fluidization times scale $\tau_\alpha = 3.5 \pm 0.7$ hr and $\tilde{d}_{xx}(t = 0)/\langle a \rangle = 0.041 \pm 0.001$.

-
- [1] Carl-Philipp Heisenberg and Yohanns Bellaïche, “Forces in tissue morphogenesis and patterning,” *Cell* **153**, 948–962 (2013).
- [2] Agustí Brugués, Ester Anon, Vito Conte, Jim H. Veldhuis, Mukund Gupta, Julien Colombelli, José J. Muñoz, G. Wayne Brodland, Benoit Ladoux, and Xavier Trepat, “Forces driving epithelial wound healing,” *Nature Physics* **10**, 683–690 (2014).
- [3] Loïc LeGoff and Thomas Lecuit, “Mechanical forces and growth in animal tissues,” *Cold Spring Harbor Perspectives in Biology* **8**, a019232 (2016).
- [4] Frank Jülicher and Suzanne Eaton, “Emergence of tissue shape changes from collective cell behaviours,” *Seminars in Cell & Developmental Biology* **67**, 103–112 (2017).
- [5] Robert J. Tetley, Michael F. Staddon, Davide Heller, Andreas Hoppe, Shiladitya Banerjee, and Yanlan Mao, “Tissue fluidity promotes epithelial wound healing,” *Nature Physics* **15**, 1195–1203 (2019).
- [6] Benoît Aigouy, Reza Farhadifar, Douglas B. Staple, Andreas Sagner, Jens-Christian Röper, Frank Jülicher, and Suzanne Eaton, “Cell Flow Reorients the Axis of Planar Polarity in the Wing Epithelium of *Drosophila*,” *Cell* **142**, 773–786 (2010).
- [7] J. Ranft, M. Basan, J. Elgeti, J.-F. Joanny, J. Prost, and F. Jülicher, “Fluidization of tissues by cell division and apoptosis,” *Proceedings of the National Academy of Sciences* **107**, 20863–20868 (2010).
- [8] Raphaël Etournay, Marko Popović, Matthias Merkel, Amitabha Nandi, Corinna Blasse, Benoît Aigouy, Holger Brandl, Gene Myers, Guillaume Salbreux, Frank Jülicher, and et al., “Interplay of cell dynamics and epithelial tension during morphogenesis of the *drosophila* pupal wing,” *eLife* **4** (2015), 10.7554/eLife.07090.
- [9] Scott Curran, Charlotte Strandkvist, Jasper Bathmann, Marc de Gennes, Alexandre Kabla, Guillaume Salbreux, and Buzz Baum, “Myosin ii controls junction fluctuations to guide epithelial tissue ordering,” *Developmental Cell* **43**, 480–492.e6 (2017), publisher: Elsevier.
- [10] Sangwoo Kim, Marie Pochitaloff, Georgina A. Stooke-Vaughan, and Otger Campàs, “Embryonic tissues as active foams,” *Nature Physics* **17**, 859–866 (2021).
- [11] William T. Gibson, James H. Veldhuis, Boris Rubinstein, Heather N. Cartwright, Norbert Perrimon, G. Wayne Brodland, Radhika Nagpal, and Matthew C. Gibson, “Control of the mitotic cleavage plane by local epithelial topology,” *Cell* **144**, 427–438 (2011).
- [12] Yanlan Mao, Alexander L Tournier, Andreas Hoppe, Lennart Kester, Barry J Thompson, and Nicolas Tapon, “Differential proliferation rates generate patterns of mechanical tension that orient tissue growth,” *The EMBO Journal* **32**, 2790–2803 (2013).
- [13] Joao Firmino, Didier Rocancourt, Mehdi Saadaoui, Chloe Moreau, and Jerome Gros, “Cell division drives epithelial cell rearrangements during gastrulation in chick,” *Developmental Cell* **36**, 249–261 (2016).
- [14] D.A. Matoz-Fernandez, Elisabeth Agoritsas, Jean-Louis Barrat, Eric Bertin, and Kirsten Martens, “Nonlinear rheology in a model biological tissue,” *Physical Review Letters* **118**, 158105 (2017).
- [15] Laura Bocanegra-Moreno, Amrita Singh, Edouard Hannezo, Marcin Zagorski, and Anna Kicheva, “Cell cycle dynamics control fluidity of the developing mouse neuroepithelium,” *Nature Physics* **19**, 1050–1058 (2023).
- [16] T. E. Angelini, E. Hannezo, X. Trepat, M. Marquez, J. J. Fredberg, and D. A. Weitz, “Glass-like dynamics of collective cell migration,” *Proceedings of the National Academy of Sciences* **108**, 4714–4719 (2011).
- [17] Jin-Ah Park, Jae Hun Kim, Dapeng Bi, Jennifer A. Mitchel, Nader Taheri Qazvini, Kelan Tantisira, Chan Young Park, Maureen McGill, Sae-Hoon Kim, Bomi Gweon, and et al., “Unjamming and cell shape in the asthmatic airway epithelium,” *Nature Materials* **14**, 1040–1048 (2015).
- [18] E.-M. Schotz, M. Lanio, J. A. Talbot, and M. L. Manning, “Glassy dynamics in three-dimensional embryonic tissues,” *Journal of The Royal Society Interface* **10**, 20130726–20130726 (2013).
- [19] Reza Farhadifar, Jens-Christian Röper, Benoit Aigouy, Suzanne Eaton, and Frank Jülicher, “The influence of cell mechanics, cell-cell interactions, and proliferation on epithelial packing,” *Current Biology* **17**, 2095–2104 (2007).
- [20] Mirjam Mayer, Martin Depken, Justin S. Bois, Frank Jülicher, and Stephan W. Grill, “Anisotropies in cortical tension reveal the physical basis of polarizing cortical flows,” *Nature* **467**, 617–621 (2010).
- [21] Isabelle Bonnet, Philippe Marcq, Floris Bosveld, Luc Fetler, Yohanns Bellaïche, and François Graner, “Mechanical state, material properties and continuous description of an epithelial tissue,” *Journal of The Royal*

- Society Interface* **9**, 2614–2623 (2012).
- [22] Karen E. Kasza, Dene L. Farrell, and Jennifer A. Zallen, “Spatiotemporal control of epithelial remodeling by regulated myosin phosphorylation,” *Proceedings of the National Academy of Sciences* **111**, 11732–11737 (2014).
- [23] Romina Piscitello-Gómez, Franz S Gruber, Abhijeet Krishna, Charlie Duclut, Carl D Modes, Marko Popović, Frank Jülicher, Natalie A Dye, and Suzanne Eaton, “Core pcp mutations affect short-time mechanical properties but not tissue morphogenesis in the *Drosophila* pupal wing,” *eLife* **12**, e85581 (2023).
- [24] Natalie A Dye, Marko Popović, K Venkatesan Iyer, Jana F Fuhrmann, Romina Piscitello-Gómez, Suzanne Eaton, and Frank Jülicher, “Self-organized patterning of cell morphology via mechanosensitive feedback,” *eLife* **10**, e57964 (2021).
- [25] Avraham Moriel, Yuri Lubomirsky, Edan Lerner, and Eran Bouchbinder, “Extracting the properties of quasilocalized modes in computer glasses: Long-range continuum fields, contour integrals, and boundary effects,” *Physical Review E* **102**, 033008 (2020).
- [26] Avraham Moriel, David Richard, Edan Lerner, and Eran Bouchbinder, “Elementary processes in dilatational plasticity of glasses,” *Physical Review Research* **6**, 023167 (2024).
- [27] Jana F. Fuhrmann, Abhijeet Krishna, Joris Paijmans, Charlie Duclut, Suzanne Eaton, Marko Popović, Frank Jülicher, Carl D. Modes, and Natalie A. Dye, “Active shape programming drives drosophila wing disc eversion,” (2023), [10.1101/2023.12.23.573034](https://doi.org/10.1101/2023.12.23.573034).
- [28] Matthias Merkel, Raphaël Etournay, Marko Popović, Guillaume Salbreux, Suzanne Eaton, and Frank Jülicher, “Triangles bridge the scales: Quantifying cellular contributions to tissue deformation,” *Physical Review E* **95** (2017), [10.1103/PhysRevE.95.032401](https://doi.org/10.1103/PhysRevE.95.032401).
- [29] John Douglas Eshelby, “The determination of the elastic field of an ellipsoidal inclusion, and related problems,” *Proceedings of the royal society of London. Series A. Mathematical and physical sciences* **241**, 376–396 (1957).
- [30] Alexandre Nicolas, Ezequiel E. Ferrero, Kirsten Martens, and Jean-Louis Barrat, “Deformation and flow of amorphous solids: Insights from elastoplastic models,” *Reviews of Modern Physics* **90** (2018), [10.1103/RevModPhys.90.045006](https://doi.org/10.1103/RevModPhys.90.045006).
- [31] We consider only force dipoles that do not exert a net torque.
- [32] Michael F. Staddon, Arthur Hernandez, Mark J. Bowick, Michael Moshe, and M. Cristina Marchetti, “The role of non-affine deformations in the elastic behavior of the cellular vertex model,” *Soft Matter* **19**, 3080–3091 (2023).
- [33] Note that this developmental stage precedes the pupal stage in which linear laser ablations were performed [23] and although both are fruit fly wing tissues, it is possible that tissue elastic constants have changed between the two stages.
- [34] P. J. Strzyz, M. Matejcić, and C. Norden, “Chapter Three - Heterogeneity, Cell Biology and Tissue Mechanics of Pseudostratified Epithelia: Coordination of Cell Divisions and Growth in Tightly Packed Tissues,” in *International Review of Cell and Molecular Biology*, International Review of Cell and Molecular Biology, Vol. 325, edited by Kwang W. Jeon (Academic Press, 2016) pp. 89–118, iSSN: 1937-6448.
- [35] O. Hertwig, *Das Problem der Befruchtung und der Isotropie des Eies: eine Theorie der Vererbung*, Jenaische Zeitschrift für Naturwissenschaften (Fischer, 1884).
- [36] Manuel Théry, Andrea Jiménez-Dalmaroni, Victor Racine, Michel Bornens, and Frank Jülicher, “Experimental and theoretical study of mitotic spindle orientation,” *Nature* **447**, 493–496 (2007).
- [37] Ana Lisica, Jonathan Fouchard, Manasi Kelkar, Tom P. J. Wyatt, Julia Duque, Anne-Betty Ndiaye, Alessandra Bonfanti, Buzz Baum, Alexandre J. Kabla, and Guillaume T. Charras, “Tension at intercellular junctions is necessary for accurate orientation of cell division in the epithelium plane,” *Proceedings of the National Academy of Sciences* **119**, e2201600119 (2022).
- [38] Teije C. Middelkoop, Jonas Neipel, Caitlin E. Cornell, Ronald Naumann, Lokesh G. Pimpale, Frank Jülicher, and Stephan W. Grill, “A cytokinetic ring-driven cell rotation achieves hertwig’s rule in early development,” (2023), [10.1101/2023.06.23.546115](https://doi.org/10.1101/2023.06.23.546115).
- [39] Jeppe C. Dyre, “Solid-that-flows picture of glass-forming liquids,” *arXiv* (2023), [10.48550/arXiv.2311.14460](https://arxiv.org/abs/10.48550/arXiv.2311.14460).
- [40] Misaki Ozawa and Giulio Biroli, “Elasticity, facilitation, and dynamic heterogeneity in glass-forming liquids,” *Phys. Rev. Lett.* **130**, 138201 (2023).
- [41] Ali Tahaei, Giulio Biroli, Misaki Ozawa, Marko Popović, and Matthieu Wyart, “Scaling description of dynamical heterogeneity and avalanches of relaxation in glass-forming liquids,” *Phys. Rev. X* **13**, 031034 (2023).
- [42] Benoit Aigouy, Daiki Umetsu, and Suzanne Eaton, “Segmentation and quantitative analysis of epithelial tissues,” in *Drosophila: Methods and Protocols*, edited by Christian Dahmann (Springer New York, New York, NY, 2016) pp. 227–239.
- [43] Raphaël Etournay, Matthias Merkel, Marko Popović, Holger Brandl, Natalie A Dye, Benoit Aigouy, Guillaume Salbreux, Suzanne Eaton, and Frank Jülicher, “Tissueminer: A multiscale analysis toolkit to quantify how cellular processes create tissue dynamics,” *eLife* **5** (2016), [10.7554/eLife.14334](https://doi.org/10.7554/eLife.14334).
- [44] Natalie A. Dye, Marko Popović, Stephanie Spannll, Raphaël Etournay, Dagmar Kainmüller, Suhrid Ghosh, Eugene W. Myers, Frank Jülicher, and Suzanne Eaton, “Cell dynamics underlying oriented growth of the drosophila wing imaginal disc,” *Development* **144**, 4406–4421 (2017).
- [45] Charlie Duclut, Joris Paijmans, Mandar M. Inamdar, Carl D. Modes, and Frank Jülicher, “Nonlinear rheology of cellular networks,” *Cells & Development* **168**, 203746 (2021).

Supplemental Information of the manuscript "Cell divisions imprint long lasting elastic strain fields in epithelial tissues"

Ali Tahaei,¹ Romina Pisticello Gómez,² S Suganthan,¹ Greta Cwikla,³
Jana F. Fuhrmann,^{2,3} Natalie A. Dye,^{2,3} and Marko Popović^{1,3,4}

¹Max Planck Institute for the Physics of Complex Systems, Nöthnitzer Str.38, 01187 Dresden, Germany

²Max Planck Institute for Molecular Cell Biology and Genetics,
Pfortenhauerstrasse 108, Dresden, 01307, Germany

³Excellence Cluster, Physics of Life, Technische Universität Dresden, Arnoldstrasse 18, Dresden, 01307, Germany

⁴Center for Systems Biology Dresden, Pfortenhauerstrasse 108, 01307 Dresden, Germany

I. CONTINUUM THEORY OF A FORCE DIPOLE PERTURBATION IN TWO DIMENSIONS

In this section, we derive the strain field generated by a force dipole described located at the origin. Force dipole is fully described by the force dipole tensor d_{ij} . First, we consider an elastic medium and we derive the steady state strain field. Then, we consider the relaxation dynamics to the steady state and compare viscoelastic and frictional relaxations as two sources of dissipation processes.

The strain field is given by $u_{ij} = (\partial_i u_j + \partial_j u_i)/2$, where u_i is the displacement field. The strain field can be decomposed as

$$u_{ij} = \frac{1}{2} u_{kk} \delta_{ij} + \tilde{u}_{ij}, \quad (1)$$

where $u_{kk}/2$ is the isotropic strain and \tilde{u}_{ij} is the shear strain. Similarly, for a symmetric force dipole, we write

$$D_{ij} = D_0 \delta_{ij} + \tilde{D}_{ij}, \quad (2)$$

with D_0 the isotropic force dipole and \tilde{D}_{ij} the traceless symmetric part of the force dipole. A schematic representation of strain field and force dipole decompositions is presented in Fig.1 (B.i).

A. Strain field of a force dipole: steady state

We start by writing the force balance equation

$$\partial_j \sigma_{ij} + f_i = 0, \quad (3)$$

where σ_{ij} is the stress tensor and the force density of the force dipole is given by

$$f_i = \partial_j [\delta(\vec{r}) D_{ij}]. \quad (4)$$

The constitutive linear elasticity equations are

$$P = -\frac{\bar{K}}{2} u_{kk}, \quad (5)$$

$$\tilde{\sigma}_{ij} = 2K \tilde{u}_{ij}, \quad (6)$$

where $P = -\sigma_{kk}/2$ is the two-dimensional pressure, $\tilde{\sigma}_{ij}$ is traceless-symmetric component of the stress tensor and

we denote it shear stress, and \bar{K} and $2K$ are bulk and shear modulus, respectively. Solving Eqs. 5 & 6 and Eq. 3 in Fourier space as we find the strain field to be

$$u_{kk} = -\frac{1}{K} \frac{\mu}{1 + \mu} \frac{q_i q_j D_{ij}}{q^2} \quad (7)$$

$$\tilde{u}_{ij} = -\frac{1}{2K} \frac{D_{kl} q_l}{q^2} \left\{ q_i \delta_{jk} + q_j \delta_{ik} - \frac{q_k}{1 + \mu} \left[\mu + \frac{2q_i q_j}{q^2} \right] \right\}, \quad (8)$$

where q_i are the Fourier wavevectors, $q^2 = q_x^2 + q_y^2$ and $\mu = 2K/\bar{K}$. Finally, we apply the inverse Fourier transform to find strain field in the real space, given by Eq. 2 in the main text. It is convenient to express the strain field using a Voigt-type of tensor representation

$$\begin{pmatrix} u_{kk}(\vec{r}) \\ \tilde{u}_{xx}(\vec{r}) \\ \tilde{u}_{xy}(\vec{r}) \end{pmatrix} = \frac{1}{2\pi K(1 + \mu)} \mathbf{G}(\vec{r}) \begin{pmatrix} D_0 \\ \tilde{D}_{xx} \\ \tilde{D}_{xy} \end{pmatrix}, \quad (9)$$

where

$$\mathbf{G}(\vec{r}) = \frac{1}{r^2} \begin{pmatrix} \mathcal{N} & -\mu \cos 2\varphi & -\mu \sin 2\varphi \\ -\mu \cos 2\varphi & -\cos 4\varphi & -\sin 4\varphi \\ -\mu \sin 2\varphi & -\sin 4\varphi & \cos 4\varphi \end{pmatrix}, \quad (10)$$

and \mathcal{N} is zero in an infinite system and a constant in a finite system. Elements of the propagator matrix $\mathbf{G}(\vec{r})$ are shown in Fig. 1 (B.iii). We define the normalized force dipole as

$$\mathbf{d} \equiv \frac{\mathbf{D}}{2\pi K(1 + \mu)}, \quad (11)$$

which will be the value that we obtain by fitting the linear elastic theory to experimental data. Namely, since our experimental measurements are purely geometric we can only determine force dipoles and stress fields normalized by the appropriate elastic constants.

B. Strain field of a force dipole: relaxation

We consider two sources of dissipation in an elastic sheet: viscosity and friction. For each of these cases, we study the strain field relaxation and we discuss how to distinguish these two different dissipation mechanisms from strain field relaxation dynamics.

1. Frictional dissipation

We introduce a friction term $-\zeta\dot{u}_i$ as the source of dissipation in the force balance equation. Then, from the force balance we have

$$-\partial_i P + \partial_j \tilde{\sigma}_{ji} + f_i - \zeta\dot{u}_i = 0. \quad (12)$$

After combining Eqs. 5 & 6, and Eq. 12, we find

$$\frac{\bar{K}}{2}\partial_i u_{kk} + 2K\partial_k \tilde{u}_{ik} + f_i - \zeta\dot{u}_i = 0, \quad (13)$$

and in the Fourier space we find the solutions

$$u_{kk} = -\frac{1}{K} \frac{\mu}{1+\mu} \frac{q_i q_j D_{ij}}{q^2} (1 - e^{-q^2 t/\beta_1}), \quad (14)$$

and

$$\begin{aligned} \tilde{u}_{ij} = & -\frac{1}{2K} \frac{q_m D_{lm}}{q^2} \times \\ & \left\{ \left[q_i \delta_{jl} + q_j \delta_{il} - 2 \frac{q_i q_j q_l}{q^2} \right] (1 - e^{-q^2 t/\beta_2}) \right. \\ & \left. - \frac{\mu}{1+\mu} q_l \left[\delta_{ij} - \frac{q_i q_j}{q^2} \right] (1 - e^{-q^2 t/\beta_1}) \right\}. \end{aligned} \quad (15)$$

Here, $\beta_1 = \frac{\zeta}{K} \frac{\mu}{1+\mu}$ and $\beta_2 = \frac{\zeta}{K}$. The relaxation terms in Eqs. 14 & 15 depend on q , so that length scale on which the system has relaxed will change in time i.e. the strain field propagates through space in time. To illustrate this, we plot the second angular mode of the strain field component $\tilde{u}_{xy}(r, m=2, t)$ in Fig. 2 (A.ii), which clearly shows a propagating front. Beyond the front the strain field rapidly vanishes and inside the front it has relaxed to the steady state value.

2. Viscoelastic relaxation

We use a Kelvin-Voigt type of material equation to introduce viscous dissipation in the model of elastic sheet. The constitutive equations are

$$P = -\frac{\bar{K}}{2} u_{kk} - \frac{\bar{\eta}}{2} \dot{u}_{kk}, \quad (16)$$

$$\tilde{\sigma}_{ij} = 2K \tilde{u}_{ij} + 2\eta \dot{\tilde{u}}_{ij}. \quad (17)$$

Here, \bar{K} and $\bar{\eta}$ are bulk modules and bulk viscosity, $2K$ and 2η are shear modules and shear viscosity, and $\dot{\mathbf{u}}$ shows the temporal derivative of the strain field. After combining Eqs. 16 & 17, and Eq. 3, we find

$$\frac{\bar{K}}{2}\partial_i u_{kk} + \frac{\bar{\eta}}{2}\partial_i \dot{u}_{kk} + 2K\partial_k \tilde{u}_{ij} + 2\eta\partial_k \dot{\tilde{u}}_{ij} - f_i = 0. \quad (18)$$

We solve Eq. 18 in Fourier space and find the transient isotropic and shear strain as,

$$u_{kk} = -\frac{1}{K} \frac{\mu}{1+\mu} \frac{q_i q_j D_{ij}}{q^2} (1 - e^{-t/\tau_1}) \quad (19)$$

$$\begin{aligned} \tilde{u}_{ij} = & -\frac{1}{2K} \frac{D_{kl} q_l}{q^2} \left\{ \left[q_i \delta_{jk} + q_j \delta_{ik} - \frac{2q_i q_j q_k}{q^2} \right] (1 - e^{-t/\tau_2}) \right. \\ & \left. - \frac{\mu}{1+\mu} q_k \left[1 - \frac{2q_i q_j}{q^2} \right] (1 - e^{-t/\tau_1}) \right\}, \end{aligned} \quad (20)$$

with two timescales $\tau_1 = \frac{\bar{\eta}}{K} \frac{1+\mu^*}{1+\mu}$ and $\tau_2 = \eta/K$, where $\mu^* = 2\eta/\bar{\eta}$. Unlike the case with friction, the relaxation factors do not depend on q which means that there is no propagating front and the spatial profile of the strain field only changes in magnitude but not in shape. After applying the inverse Fourier transformation to Eqs. 19 & 20, and together with Eq. 11 we find that,

$$\begin{pmatrix} u_{kk} \\ \tilde{u}_{xx} \\ \tilde{u}_{xy} \end{pmatrix} = \mathbf{G}(\mathbf{r}, t) \begin{pmatrix} d_0 \\ \tilde{d}_{xx} \\ \tilde{d}_{xy} \end{pmatrix}. \quad (21)$$

Here, \mathbf{G} is the matrix whose components are given by $G_{ij}(\mathbf{r}, t) = G_{ij}(\mathbf{r})T_{ij}(t)$, where no sum over repeated indices is performed. $G_{ij}(\mathbf{r})$ is the elastic kernel from Eq. 10, $T_{ij}(t)$ are components of matrix \mathbf{T}

$$\mathbf{T} = \begin{pmatrix} g_1(t) & g_1(t) & g_1(t) \\ g_1(t) & (1+\mu)g_2(t) - \mu g_1(t) & (1+\mu)g_2(t) - \mu g_1(t) \\ g_1(t) & (1+\mu)g_2(t) - \mu g_1(t) & (1+\mu)g_2(t) - \mu g_1(t) \end{pmatrix}, \quad (22)$$

where,

$$g_1(t) = 1 - e^{-t/\tau_1}, \quad (23)$$

$$g_2(t) = 1 - e^{-t/\tau_2}. \quad (24)$$

Our results show that there is a qualitative difference in the dynamics of strain field relaxation between frictional and viscous dissipation mechanisms. During the viscous relaxation of an elastic sheet radial dependence of the strain field is given by $1/r^2$ at all times, as shown in Eq. 21, whereas during frictional relaxation a propagation front appears. We show the radial profile of $\tilde{u}_{xy}(r, m=2, t)$ for viscous and frictional relaxation in Fig. 2 A. Therefore, presence of a propagating front would be a signature of frictional dissipation. However, we do not find any sign of such a front in experimentally measured strain fields, which suggests that the dominant dissipation mechanism in the *D. melanogaster* pupal wing epithelium is viscous.

Finally, to determine the viscous relaxation timescales we fit Eq. 21 to the measured transient strain field at each timepoint t_i . Since we have already determined the normalized force dipole tensor \mathbf{d} and μ , this allows us to find $g_1(t_i)$ and $g_2(t_i)$. We plot the obtained values of $1 - g_1(t_i)$ and $1 - g_2(t_i)$ in SI Fig. 1. We then extract the viscous relaxation timescales τ_1 and τ_2 by fitting an exponential function to these data, see dashed lines in SI Fig. 1.

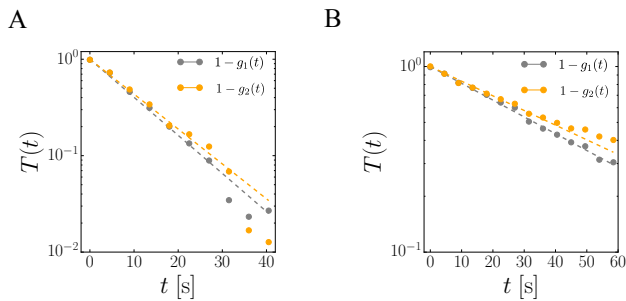


FIG. 1. Measured relaxation times from the strain fields measure $1 - g_1(t)$ and $1 - g_2(t)$. The dashed lines show the fits with the parameters reported in Table. 1. (A) shows the data from laser ablation Exp. 1 of the main text, and (B) shows Exp. 2 of the main text.

II. VERTEX MODEL IMPLEMENTATION

To simulate linear ablation we use the 2d vertex model of epithelial tissues [1]. The tissue is modeled as a tiling of polygonal cells and is endowed with the energy functional

$$W = \sum_{c \in \text{cells}} \frac{K}{2} (A_c - A_c^0)^2 + \sum_{b \in \text{bonds}} \Lambda_b L_b + \sum_{c \in \text{cells}} \frac{\Gamma_c}{2} P_c^2 \quad (25)$$

In the above expression, the first term represents the area elasticity of cells arising from the volume incompressibility of the epithelial layer; A_c , A_c^0 and K_c denote the area, preferred area and area elastic modulus of cell 'c' respectively. The second term corresponds to inter-

facial tension in the bonds arising from actomyosin contractility and adhesion between cells sharing the bond; Λ_b and L_b correspond to the bond tension parameter and the length of the bond 'b' respectively. The final term is quadratic in length resulting in a bond tension that is dependent on the perimeter of the cell; Γ_c sets the strength of the perimeter contractility and P_c is the perimeter of the cell. The degrees of freedom of the system are the vertex positions \vec{r}_v which are evolved using overdamped dynamics as follows

$$\gamma \frac{d\vec{r}_v}{dt} = -\nabla_{\vec{r}_v} W \quad (26)$$

We first prepare the sample by randomizing a hexagonal network of 2500 cells using bond tension fluctuations under periodic boundary conditions. We choose the parameters Λ and Γ such that it corresponds to a negative Poisson's ratio as reported in [2] for a hexagonal lattice. Similar values of Poisson ratio have also been measured in the *D. melanogaster* pupal wing epithelium [3]. We then apply pure shear stress to the sample to incorporate the presence of pre-stresses in the wing disc. Once the target value of the pure shear stress is reached we fix the simulation box boundaries and relax the system to the nearest energy minimum. To perform linear ablation, a single bond is removed by removing its vertices, and the two cells that originally abutted the bond are connected to form a single cell. For the new cell, we set $K_c = \Gamma_c = 0$. The removal of the bond introduces a force dipole in the tissue resulting in redistribution of stress. During this process, we record the configuration of the system and perform the same analysis as done for the experimental data.

-
- [1] Reza Farhadifar, Jens-Christian Röper, Benoit Aigouy, Suzanne Eaton, and Frank Jülicher, "The influence of cell mechanics, cell-cell interactions, and proliferation on epithelial packing," *Current Biology* **17**, 2095–2104 (2007).
- [2] Michael F. Staddon, Arthur Hernandez, Mark J. Bowick, Michael Moshe, and M. Cristina Marchetti, "The role of non-affine deformations in the elastic behavior of the cellular vertex model," *Soft Matter* **19**, 3080–3091 (2023).
- [3] Romina Piscitello-Gómez, Franz S Gruber, Abhijeet Krishna, Charlie Duclut, Carl D Modes, Marko Popović, Frank Jülicher, Natalie A Dye, and Suzanne Eaton, "Core pcp mutations affect short-time mechanical properties but not tissue morphogenesis in the *Drosophila* pupal wing," *eLife* **12**, e85581 (2023).

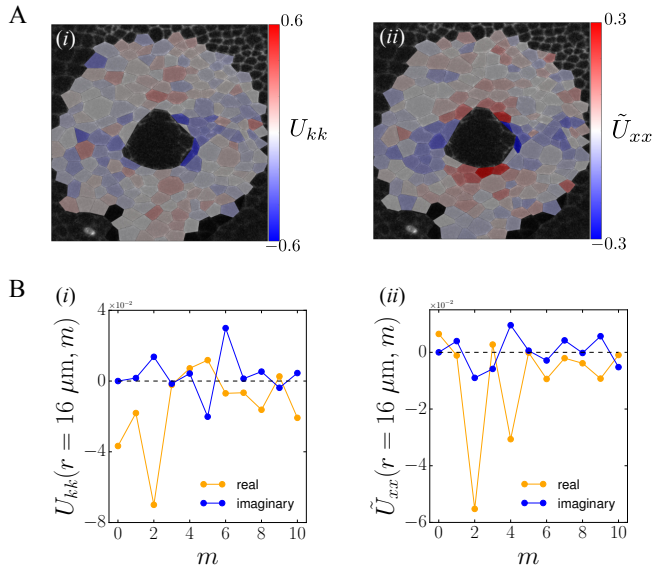


FIG. 2. (A) Components kk and xx of the strain field generated by a linear laser ablation in experiment 1. (B) Angular Fourier modes of the strain field from experiment 1 show strongest signal in modes $m = 0$ and $m = 2$ for U_{kk} strain component, and modes $m = 2$ and $m = 4$ for U_{xx} component. Real and imaginary parts of Fourier modes correspond to $\cos(m\varphi)$ and $\sin(m\varphi)$ angular profiles, respectively.

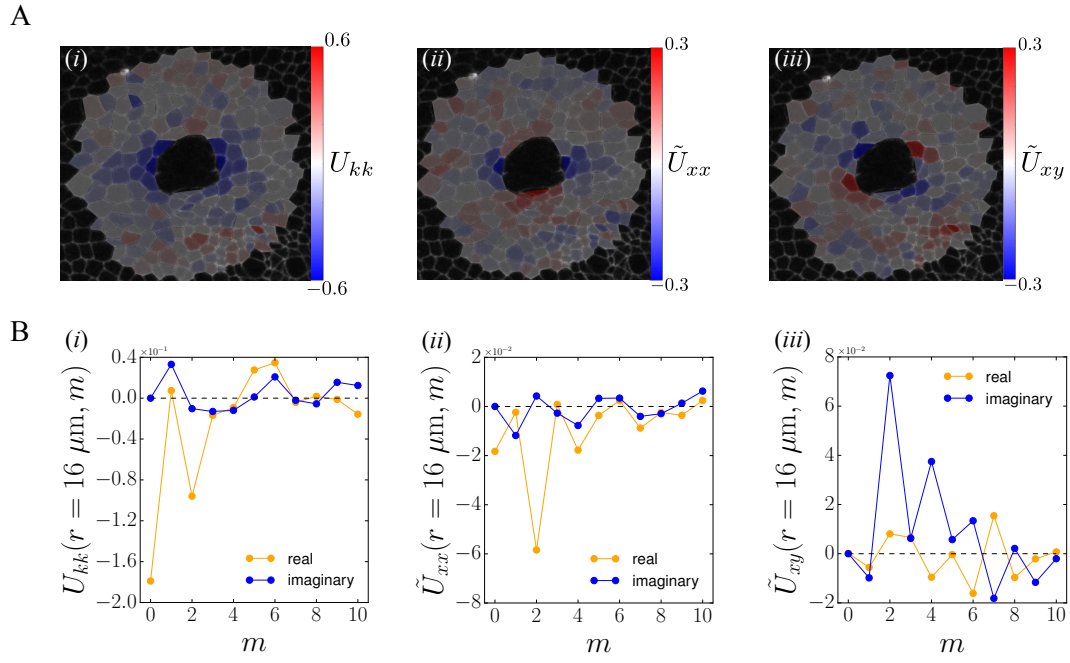


FIG. 3. (A) All components of the strain field generated by a linear laser ablation in experiment 2. (B) Angular Fourier modes of the strain field from experiment 2 show strongest signal in modes $m = 0$ and $m = 2$ for U_{kk} strain component, and modes $m = 2$ and $m = 4$ for U_{xx} and U_{xy} components. Real and imaginary parts of Fourier modes correspond to $\cos(m\varphi)$ and $\sin(m\varphi)$ angular profiles, respectively.

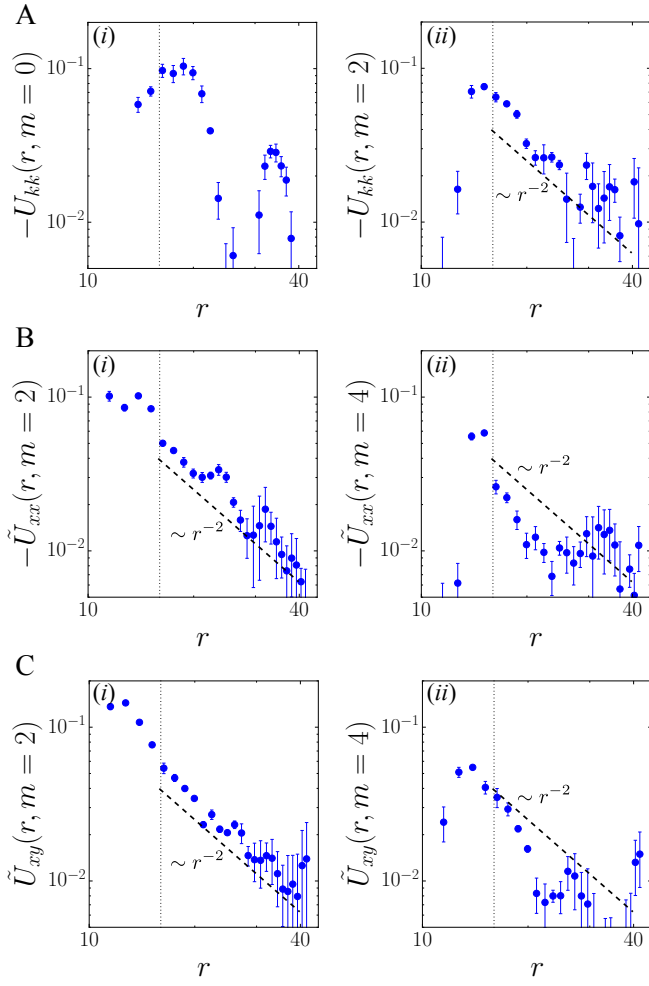


FIG. 4. Radial dependence of strain field components angular Fourier modes, measured in experiment 1. Vertical dotted line indicates $r = 16\mu m$. Dashed line indicates r^{-2} decay for comparison, where appropriate. (A) Modes $m = 0$ and $m = 2$ of the strain component kk . (B) Modes $m = 0$ and $m = 2$ of the strain component xx . (C) Modes $m = 0$ and $m = 2$ of the strain component kk .

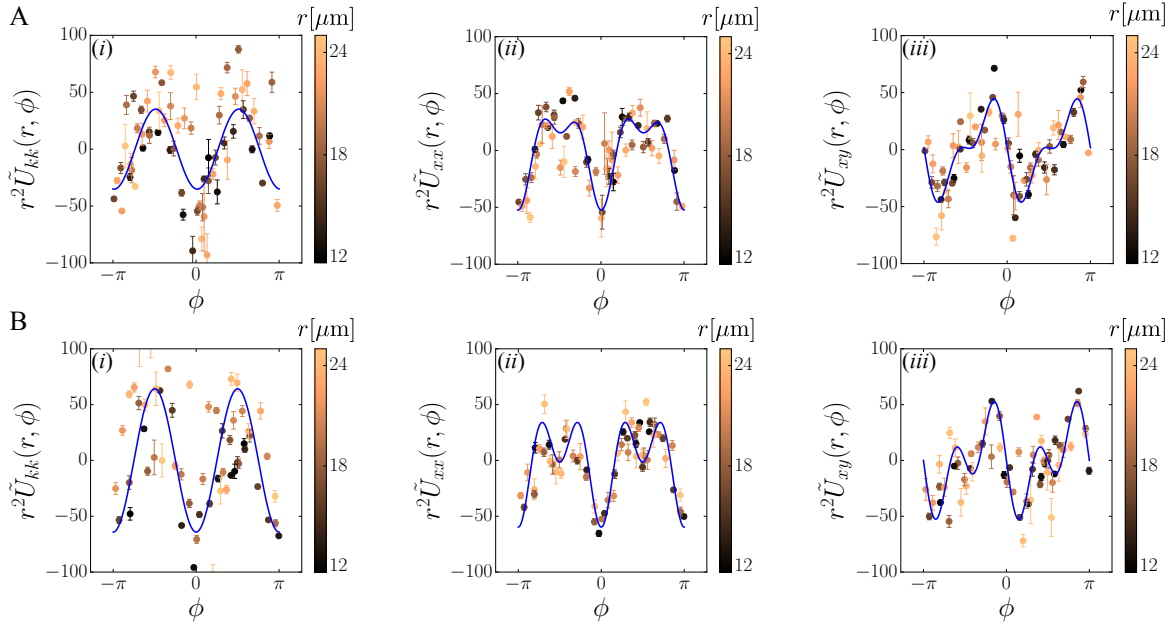


FIG. 5. Blue line shows the fit of the linear elastic theory to the data points representing the strain field measured in laser ablation experiments. Data at different radial distances from the ablation are shown in different colors as indicated by the colorbar. Error bars indicate the standard deviation of measured strain values in corresponding radial/angular bin. (A) Shear strain components measured in experiment 1 and corresponding best fit of the theory. (B) Shear strain components measured in experiment 2 and corresponding best fit of the theory.

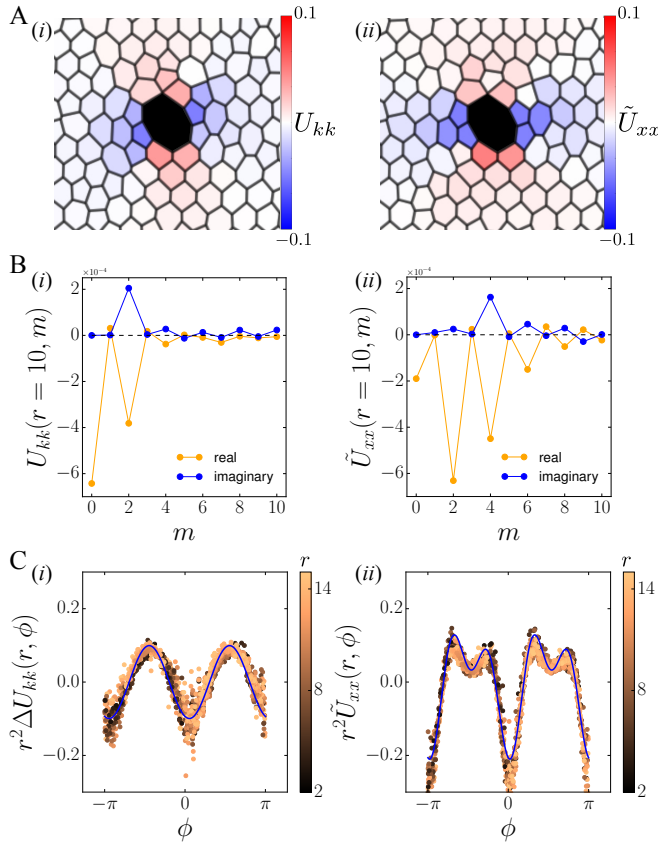


FIG. 6. (A) Steady state strain field components U_{kk} and \tilde{U}_{xx} generated by a laser ablation simulation in the vertex model. (B) Angular Fourier modes of the strain field components show strongest signal in modes $m = 0$ and $m = 2$ for U_{kk} strain component, and modes $m = 2$ and $m = 4$ for U_{xx} component. Real and imaginary parts of Fourier modes correspond to $\cos(m\varphi)$ and $\sin(m\varphi)$ angular profiles, respectively. (C) Blue line shows the fit of the linear elastic theory to the data points representing the strain field measured in laser ablation experiments. Data at different radial distances from the ablation are shown in different colors as indicated by the colorbar. Data points correspond to strain measured in individual cells in the vertex model.

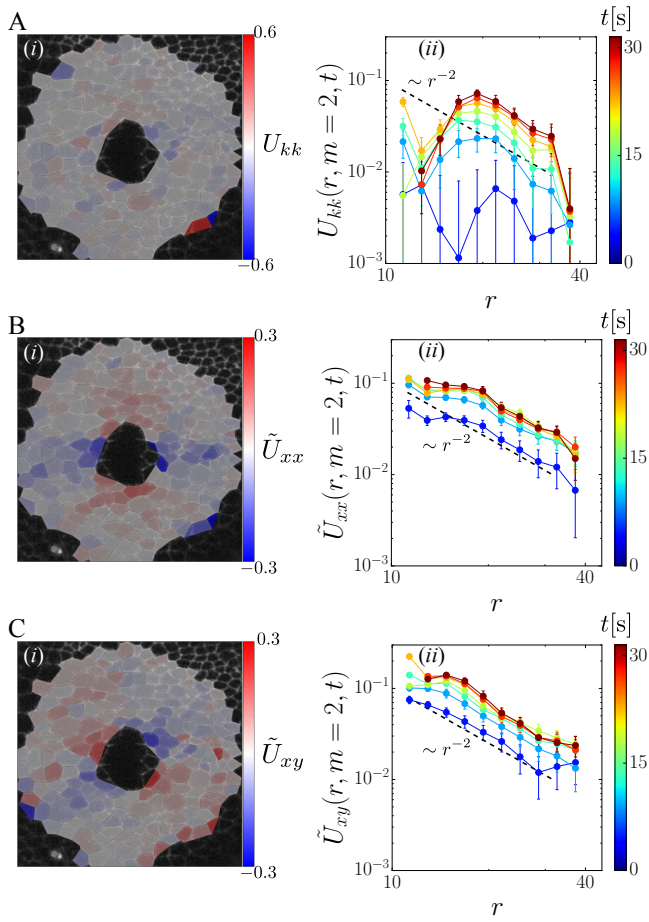


FIG. 7. Time evolution of the strain field induced by the laser ablation in experiment 1. Each panel shows a component of the strain field after relaxation on the left and radial dependence of the second Fourier mode on the right. (A) U_{kk} component, (B) \tilde{U}_{xx} component and (C) \tilde{U}_{xy} component. Dashed line shows a power-law decay r^{-2} for reference.

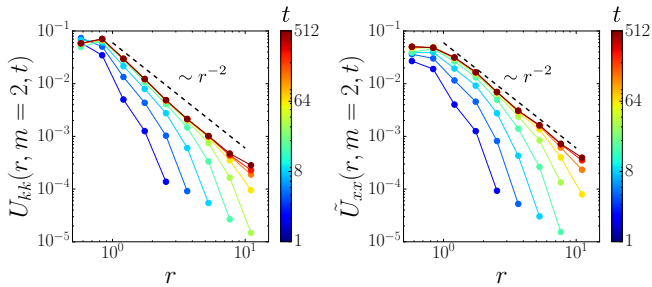


FIG. 8. Time evolution the second Fourier mode $m = 2$ of the strain field components kk and xx , induced by laser ablation in vertex model simulation with frictional dissipation. Dashed line indicates the power-law r^{-2} decay for reference.